High-throughput Screening of Nitrogen Coordinated Bi-metal Catalysts for Multielectron Reduction of CO_2 to CH_4 with High Selectivity and Low Limiting Potential

Shuo Wang[a], Lei Li[b,*], Jing Li[a], Chengzong Yuan[a], Yao Kang[a], Kwan San Hui[c,*], Jintao Zhang[d], Feng Bin[e], Xi Fan[f], Fuming Chen[g,*], Kwun Nam Hui[a,*]

[a] Joint Key Laboratory of the Ministry of Education, Institute of Applied Physics and Materials Engineering, University of Macau, Avenida da Universidade, Taipa, Macau SAR, P.R. China. Email: bizhui@um.edu.mo

[b] Hefei National Laboratory for Physical Sciences at the Microscale, Collaborative Innovation Center of Chemistry for Energy Materials, University of Science and Technology of China, Hefei, 230026, P.R. China. Email:uestclilei@163.com

[c] School of Engineering, Faculty of Science, University of East Anglia, Norwich, NR4 7TJ, United Kingdom. Email: k.hui@uea.ac.uk

[d] School of Chemistry and Chemical Engineering, Shandong University, Jinan, 250100, P.R. China

[e] State Key Laboratory of High-Temperature Gas Dynamics, Institute of Mechanics, Chinese Academy of Sciences, Beijing, 100190, P.R. China

[f] Ningbo Institute of Materials Technology, Engineering, Chinese Academy of Sciences, Ningbo, 315201, P.R. China

[g] Guangdong Provincial Key Laboratory of Quantum Engineering and Quantum Materials, School of Physics and Telecommunication Engineering, South China Normal University, Guangdong, 510006, P.R. China. E-mail: fmchen@m.scnu.edu.cn

1 **Abstract**

2   Significant challenges remain for developing efficient catalysts in electrochemical

3 multielectron CO_2 reduction reaction (CO_2RR), which usually suffer from poor activity

4 and selectivity. Motivated by the recent experimental progress in fabricating dual-metal

5 atoms catalysts (DMACs) in N-doped graphene materials (graphene-N6V4; N: nitrogen,

6 V: vacancy), we sampled 8 types of homonuclear (N6V4-M_2, M = Cr, Mn, Fe, Co, Ni,

7 Cu, Pd, and Ag) catalysts and 28 types of heteronuclear (N6V4-M1M2) catalysts to

8 study CO_2RR activity via first-principles high-throughput screening. Using stability,

9 activity, and selectivity as indicators along with broken the conventional scaling

10 relationship, N6V4-AgCr was selected as a promising candidate for deep CO_2 reduction

11 to methane with a low overpotential of 0.55 V after two screening rounds. Further

12 analysis showed that a frustrated Lewis pair, formed between metal and the para-N,

13 owing to the difference in the electronic arrangement of the d-orbitals of various

14 transition metals, which caused a difference in the spin polarization of the systems and

15 affected the catalytic performance of each DMAC. Our work not only provides a solid

16 strategy for screening potential catalysts but also demonstrates that their CO_2 reduction

17 activities originate from the various atomic and electronic structures of DMACs.

18   **Keywords:** Electrocatalysis, Density functional theory (DFT) calculations, CO_2

19 reduction reaction, Dual atom catalysts, Spin polarization

20

1. Introduction

The growing demand of fossil fuels is accompanied by excessive emissions of CO_2, resulting in serious climate change with harmful environment and health impacts. Thus, it is of vital urgency to seek effective methods for reducing CO_2 content, converting CO_2 to fuels, and further closing the anthropogenic C cycle. Electrochemical CO_2 reduction reaction (CO_2RR) is regarded as a promising approach for managing global C balance and converting CO_2 to value-added C-based products.[1-2] In particular, CO_2RR can produce several C1 products including carbon monoxide (CO), formic acid (HCOOH), methanol (CH_3OH), and methane (CH_4). All the C1 products are of highly relevant to chemical industry.[3-5] However, the previous studies mainly focus on the 2 electrons reduction process, such as the reduction of CO_2 to CO or HCOOH.[6-9] The practical implementation of multi-electrons reduction of CO_2 faces major hurdles due to energy efficiency and product selectivity.[10-11] In this regard, exploring robust catalysts for deep CO_2 reduction with high activity and selectivity is still a truly novel undertaking.[12]

Transition metals (denoted as M) are the most common choice for CO_2RR electrocatalysts. To date, Cu-based materials has been demonstrated as the most wildly investigated metal catalyst for CO_2 reduction toward deeper reduction products.[10, 13] However, the conventional linear scaling relations between the adsorption strengths of reaction intermediates on the pure metal surface greatly limits the exploration of superior catalysts toward other metal catalysts.[14-15] Generally, pure metal materials cannot effectively activate CO_2 due to the scaling relations unless a prohibitively high overpotential of -1 V is used to initiate the reaction.[16] In addition, the hydrogen evolution reaction (HER) can be easily dominated under the same conditions,

1   diminishing the efficiency of CO_2RR.[2, 17-18] Therefore, a wide-spread approach is to

2   make the atomic-level manipulation of metal atoms for designing highly active

3   electrocatalysts. To solve the problems of reactivity and selectivity, recently, some

4   single metal catalysts (SACs) have been widely studied.[19-20] However, the catalytic

5   activity of single atom catalyst is usually limited to the low density of metal active site,

6   couple with relatively simple electronic structure.[21] Meanwhile, the single metal atoms

7   tend to form cluster during synthesis, leading to the challenging for efficient use of

8   single atomic catalysts.[22-23]

9   In this case, dual-metal atoms catalysts (DMACs), with $M1M2-N_x-C$ coordination,

10   have elicited considerable attention in heterogeneous catalysis because of their unique

11   atomic and electronic structures compare to SACs. DMACs impose mutual effects for

12   tuning the electronic structures of both M sites, altering the binding energy of reaction

13   intermediates. Such effects reduce the energy barrier and improve the reaction rate

14   through an efficient and stable approach.[24-26] The electrochemical applications of

15   DMACs have been used toward multi-intermediate electrochemical reactions, such as

16   the oxygen reduction/evolution reaction (ORR/OER),[27-30] CO_2RR,[26, 31-34] and N_2

17   reduction reaction (NRR).[35-37] In the applications of CO_2RR field, several researchers

18   have successfully prepared DMACs in C-based materials and suggested DMACs as a

19   potential alternative to Cu as electrocatalysts for CO_2RR.[30, 38-43] For example, Ren et al.

20   synthesized a novel electrocatalyst with Fe-Ni dual sites embedded into N-doped

21   porous C as an efficient catalyst for CO_2RR.[44] By utilizing the strong adsorption of CO_2

22   molecules on Fe and the weak binding capacity of Ni with CO, the selectivity of the

23   DMAC for CO_2RR toward CO achieves an impressive high selectivity of 99%, Faraday

efficiency (FE) exceeds 90% in a wide potential range, ranging from -0.5 to -0.9 V,

reaching 98% at −0.7 V compared with a reversible H electrode (RHE). Two recent

studies also successfully identified high activity catalysts for CO_2RR by breaking down

the severe restriction imposed by scaling relations on catalytic activity.[26, 34] Significant

activity and selectivity for CO have also been observed in Cu/Mn, Ni/Mn, and Ni/Fe

DMACs via theoretical computations. The results are even better than that of the well-

established metal catalyst due to the breaking of the scaling relationship between the

adsorption strength of *CO and *COOH species (* indicates the active site).[34] Despite

their superior activity, some questions regarding DMACs remain unanswered. First,

given that the combination of two different transition metal atoms has many

possibilities, can theoretical calculations screen out experimentally unexplored

DMACs with remarkable CO_2RR catalytic performance? Second, what are the

fundamental factors that determine the catalytic activity of DMACs? Answering these

questions can identify potential good catalysts for CO_2RR and provide guidelines for

designing highly efficient DMACs for CO_2RR and other electrochemical reactions.

In this work, high-throughput DFT calculations were conducted to investigate

several transition metals (M = Cr, Mn, Fe, Co, Ni, Cu, Pd, and Ag) homonuclear and

heteronuclear dual-metal atoms embedded into a series of N-doped graphene-based

catalysts (denoted as N6V4-M_2 or N6V4-M1M2, as shown in **Fig. 1**). Half of the

candidates were first selected by evaluating stability, activity, and selectivity. Further

analysis was performed by breaking the scaling relationship between the adsorption

strengths of *COOH/*CHO and *CO species. Then, N6V4-AgCr was identified from

the 36 concept catalysts as a highly promising catalyst for the electrochemical CO_2

1   reduction to produce CH_4. Additional investigation showed that a frustrated Lewis pair

2   (FLP) was formed between the metal and the adjacent N due to the different spin

3   polarization in the electronic arrangement of the *d*-orbitals of various transition metals.

4   The catalytic performance was significantly dominated by the various spin polarization

5   of the screened systems.

6   **2. Models and computational methods**

7   **2.1 Models**

8   Based on the experimental characterization results of the K-edge X-ray absorption

9   near-edge structure and the extended X-ray absorption fine structure spectra,[39] a

10   rectangular superlattice of graphene to confine a pair of metal atoms with coordinated

11   N was considered. As shown in **Fig. 1**, two transition metal atoms are joined in graphene

12   to replace four C vacancies, and both atoms are surrounded by three N atoms. Hence,

13   we define it as N6V4-M_2/M1M2. Geometrically, M1 and M2 are equivalent sites, and

14   thus, 28 heteronuclear N6V4-M1M2 and 8 homonuclear N6V4-M_2 were calculated in

15   our work.

16
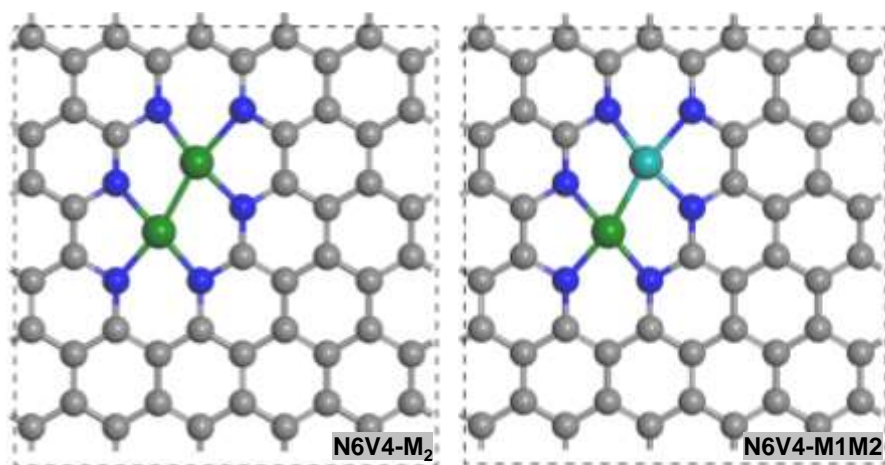
1   **Fig. 1.** Schematic of the geometric structure of N6V4-M1M2 and N6V4-M_2. The gray and blue

2   balls represent C and N atoms, respectively, and the cyan and green balls represent the two

3   transition metal atoms.

4   **2.2 Computational methods**

5   All the calculations were performed on the basis of the spin-polarized DFT[45]

6   methods implemented in the Vienna Ab initio Simulation Package (VASP 6.0).[46] The

7   generalized gradient approximation was used to estimate exchange–correlation

8   interaction [47] in the scheme of the Perdew–Burke–Ernzerhof functional.[48] The effect of

9   core electrons on the density of valence electrons was described using the projector

10   augmented wave method.[49] The kinetic energy cutoff for the plane waves was set to

11   450 eV for all the calculations in the 6×6×1 graphene super cells. The convergence

12   tolerance of energy and force on each atom during structure relaxation were less than

13   10^{-4} eV and 0.02 eV/Å, respectively. A set of Monkhorst–Pack mesh K points of 3×3×1

14   and 5×5×1 are used to sample the Brillouin zone for geometry optimization and

15   electronic structural calculations.[50] A vacuum distance of 20 Å was set for graphene to

16   ensure sufficient vacuum and avoid interactions between two periods. The thermal and

17   zero-point energy (ZPE) corrections of different C intermediates adsorbed onto

18   graphene were further calculated at the Γ point. Grimme's dispersion-corrected DFT

19   scheme was used to describe the van der Waals interactions in the systems.[51-52]

20   The free energy (G) of each reaction intermediate was given as $G = E_{DFT} +$

21    $E_{ZPE} - TS$, where E_{DFT} is DFT calculated electronic energy; and E_{ZPE} and S are the

22   ZPE correction and the entropy, respectively. T is the temperature, and it was set to

23   298.15 K. At electrode potential U = 0 V (versus RHE), the change of free energy (ΔG)

24   can be calculated using the following equation:$\Delta G = \Delta E + \Delta ZPE - T\Delta S$, where ΔE is

1 the reaction energy of hydrogenation; and ΔE_{ZPE} and ΔS are the difference of E_{ZPE} and

2 S, respectively. The E_{ZPE} and TS for all the intermediates of CO_2 reduction on N6V4-

3 M_2/M1M2 are calculated by the following equations

$$E_{ZPE} = \frac{1}{2} \sum_i h v_i \tag{1}$$

$$-TS = K_B T \sum_i \ln\left(1 - e^{-\frac{h v_i}{K_B T}}\right) - \sum_i h v_i \left(\frac{1}{e^{\frac{h v_i}{K_B T}} - 1}\right) \tag{2}$$

7   where h, v and K_B represent Planck constant, vibrational frequencies and

8 Boltzmann constant, respectively.

9 **3. Results and discussion**

10 **3.1 Stability and screening methods**

11   First, we theoretically examinate the geometric structures of the aforementioned 8

12 homonuclear N6V4-M_2 and 28 heteronuclear N6V4-M1M2 monolayers. The details of

13 the optimized structures are provided in **Fig. S1** of the Supporting Information. All

14 metal atoms can be incorporated into the central cavity of graphene and form nearly in-

15 plane configurations. The distances between two metal atoms are within the range of

16 2.19 Å (for N6V4-FeCo) to 2.53 Å (for N6V4-CrMn). All metal dimers exhibit shorter

17 bond length compared with interatomic bond length in their bulk. Such interconnection

18 enables electronic conversion between dimers to synergistically react and adsorb the

19 adsorbate, triggering a different catalytic performance from the monoatomic

20 counterpart.[53]

1   Then, we evaluated the thermodynamic and electrochemical stabilities of the 36

2   N6V4-M_2/M1M2 monolayers through their formation energy E_f and dissolution

3   potential U_{diss} (**Fig. 2a**),[54] which are defined as $E_{f} = (E_{total} - E_{N6V4} - 2E_M)/2$ and

4      $U_{diss} = U_{diss}^{\circ}(metal, bulk) - \frac{E_f}{ne}$ for homonuclear, where E_M is the total energy of

5   the metal atoms in the most stable bulk structure; E_{total} and E_{N6V4} are the total energies

6   of N6V4-M_2/M1M2 and the substrate, respectively; U_{diss}° (metal, bulk) is the standard

7   dissolution potential of the bulk metal and n is the number of electrons involved in the

8   dissolution. For heteronuclear, both two different metals are discussed at the same time,

9   which are defined as $E_f = E_{total} - E_{N6V4} - E_{M1} - E_{M2}$ and $U_{diss} =$

10     $U_{diss}^{\circ}(metal1, bulk) + U_{diss}^{\circ}(metal2, bulk) - \frac{E_f}{n1e+n2e}.$

11   In accordance with the definition provided in a previous study,[36] $E_f < 0$ eV

12   indicated thermodynamical stability, while $U_{diss} > 0$ V versus standard hydrogen

13   electrode suggested electrochemical stability. The exact values of the E_f and U_{diss} of

14   N6V4-M_2 and N6V4-M1M2 are listed in Tables S1 and S2, respectively.

15   The computed E_f values of nearly all the selected N6V4-M_2/M1M2 systems,

16   except for N6V4-Ag_2, are considerably below zero, suggesting the high thermodynamic

17   stabilities of these metal dimers in the graphene-N6V4 substrate. With regard to U_{diss},

18   half systems are excluded due to electrochemical instability under acidic conditions, as

19   indicated by their negative U_{diss} values (**Fig. 2a**).
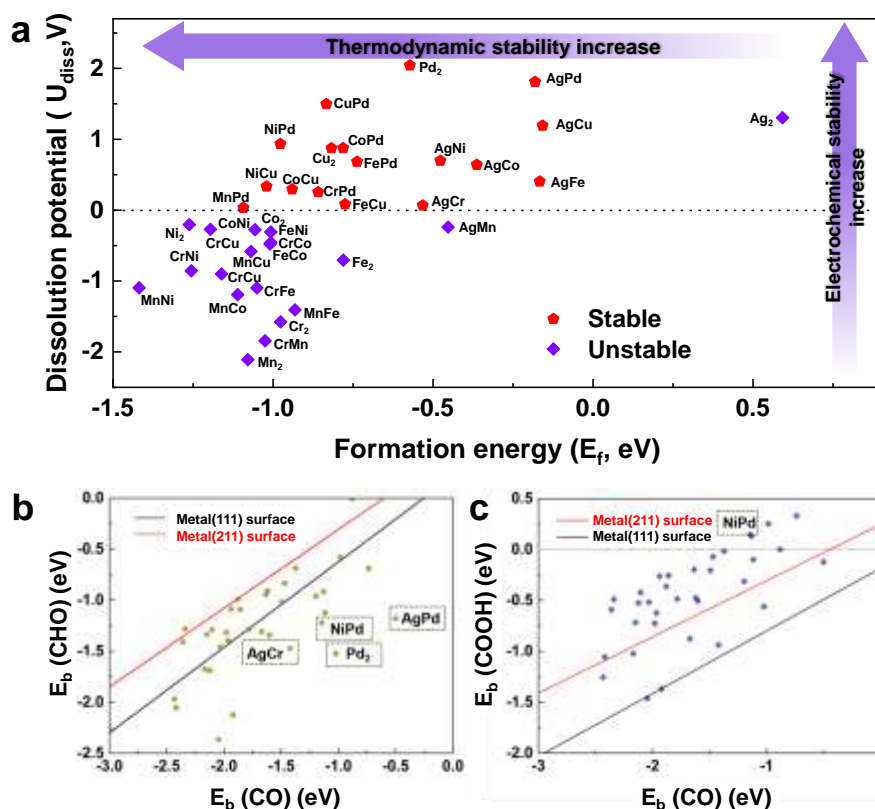
Fig. 2. (a) Computed formation energy and dissolution potential of metal atoms in N6V4-M_2/M1M2. (b–c) Relationship between the binding energies of (b) $E_b(CHO)$ and $E_b(CO)$ and (c) $E_b(COOH)$ and $E_b(CO)$ of the N6V4-M_2/M1M2 systems on the transition metal surface. Use the calculated Ni, Cu, Ag, Pd, Au, Pt and Rh data to generate a linear proportional relationship between adsorbates. [55]

Furthermore, attaining a low overpotential toward electrocatalytic CO_2RR is difficult due to adsorbate (particularly *COOH, *CO, and *CHO) scaling relations.[26, 55-56] In general, the hydrogenation of *COOH to *CO or *CO to *CHO is always the potential rate-determining step (RDS) of CO_2 reduction, and thus, the overall catalytic efficiency depends on the binding energies of *COOH [$E_b(COOH)$], *CO [$E_b(CO)$], and *CHO [$E_b(CHO)$].[55] Accordingly, we then studied *CHO, *COOH, and *CO adsorption onto N6V4-M_2/M1M2. As shown in **Figs. 2b–2c** and **S2**, the scaling

1 relations of the systems are completely different from those of pure metal surfaces.

2 Points are dispersed in the entire region between E_b (COOH) and E_b (CO), proving that

3 the diatomic systems can effectively break the traditional linear relationship. That is,

4 for the same *COOH adsorption strength, DMACs have stronger *CO adsorption

5 strength, making *COOH→*CO easier. Hence, forming *CO and approaching the

6 desired low overpotential region are easier than the other hydrogenation steps. For the

7 relationship between E_b (CHO) and E_b (CO), most systems exhibit a strong linear

8 relationship, except for the six systems that deviate significantly from the straight line,

9 namely, N6V4-Pd$_2$, N6V4-Cr$_2$, N6V4-CrCo, N6V4-AgCr, N6V4-AgPd, and N6V4-

10 NiPd. However, N6V4-Cr$_2$ and N6V4-CrCo are excluded due to their unsatisfactory

11 results in the preceding stability tests. Hence, we finally identified four systems, namely,

12 N6V4-Pd$_2$, N6V4-AgCr, N6V4-AgPd, and N6V4-NiPd, that meet the stability criteria

13 and break the aforementioned scaling relations for further investigations. We also

14 calculated the projected density of states (PDOS) of four candidates after adsorbed with

15 *CO and shown in **Fig. S3**. It can be seen clearly that there is strong bonding between

16 the *p*-orbitals of carbon atoms of the adsorbed *CO and the *d*-orbitals of dual metals at

17 the region of -7 ~ -8.5 eV below the fermi energy level. And the insert numbers of

18 electrons obtained by *CO further demonstrated the strong interaction between the *CO

19 and metal active sites.

20 **3.2 The activation of CO$_2$**

21 The activation of CO$_2$ onto the surface of catalysts is always the first step in

22 electrocatalytic CO$_2$ reduction. The structures of CO$_2$-adsorbed N6V4-M$_2$/M1M2

23 (N6V4-Pd$_2$, N6V4-AgCr, N6V4-AgPd, and N6V4-NiPd) are illustrated in **Fig. 3**. CO$_2$

24 is first adsorbed on two metal sites of all four candidates. After the optimization of these

1   candidates, CO_2 is slightly far away from the surface and then lead to physical

2   adsorption except for N6V4-AgCr. The binding strength between CO_2 and N6V4-AgCr

3   is extremely strong with an adsorption energy of −0.91 eV and the distance between

4   CO_2 and the metal of N6V4-AgCr is 2.60 Å. Meanwhile, the others are physical

5   adsorption with less negative adsorption energies of −0.45, −0.47, and −0.21 eV and

6   longer distance between CO_2 and the metal of 3.58, 3.57 and 3.33 Å for N6V4-Pd_2,

7   N6V4-AgPd, and N6V4-NiPd, respectively. The charge density difference of N6V4-

8   M_2/M1M2 with CO_2 adsorption is shown in **Fig. 3**. A significant charge transfer can be

9   observed between the anchored metal dimers and CO_2. All these findings indicate that

10 CO_2 molecules can be activated by metal dimers embedded into graphene-N6V4.
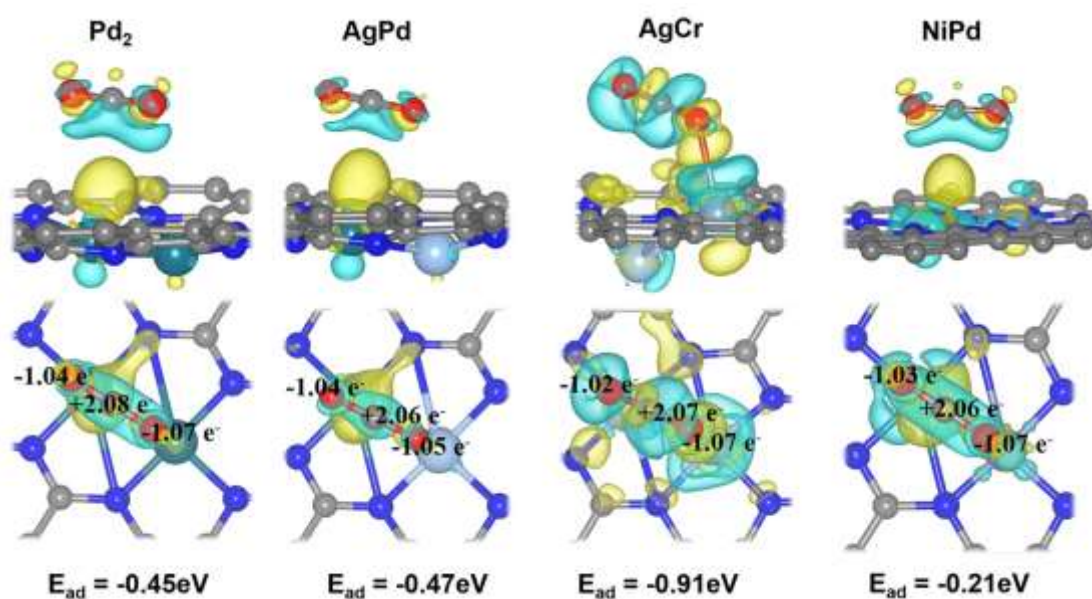
11

12 **Fig. 3.** Side and top views of the charge density difference for CO_2 adsorbed on N6V4-

13 M_2/M1M2 (N6V4-Pd_2, N6V4-AgCr, N6V4-AgPd and N6V4-NiPd). In the below figures,

14 negative values indicate the number of obtained electrons, positive values indicate the

1   number of lost electrons. Charge depletion and accumulation are presented in cyan and

2   yellow, respectively. Isosurface = 4×10^{-4} e/Å^3.

3   **3.3 Entire pathways for CO_2RR**

4   We then explored CO_2RR pathways based on N6V4-Pd$_2$, N6V4-AgCr, N6V4-

5   AgPd and N6V4-NiPd. The four candidates possess the same reaction pathways (**Fig.**

6   **4**). The detailed free energy diagrams are shown in **Fig. 5** and the related optimized

7   structures are shown in **Fig. S4**.
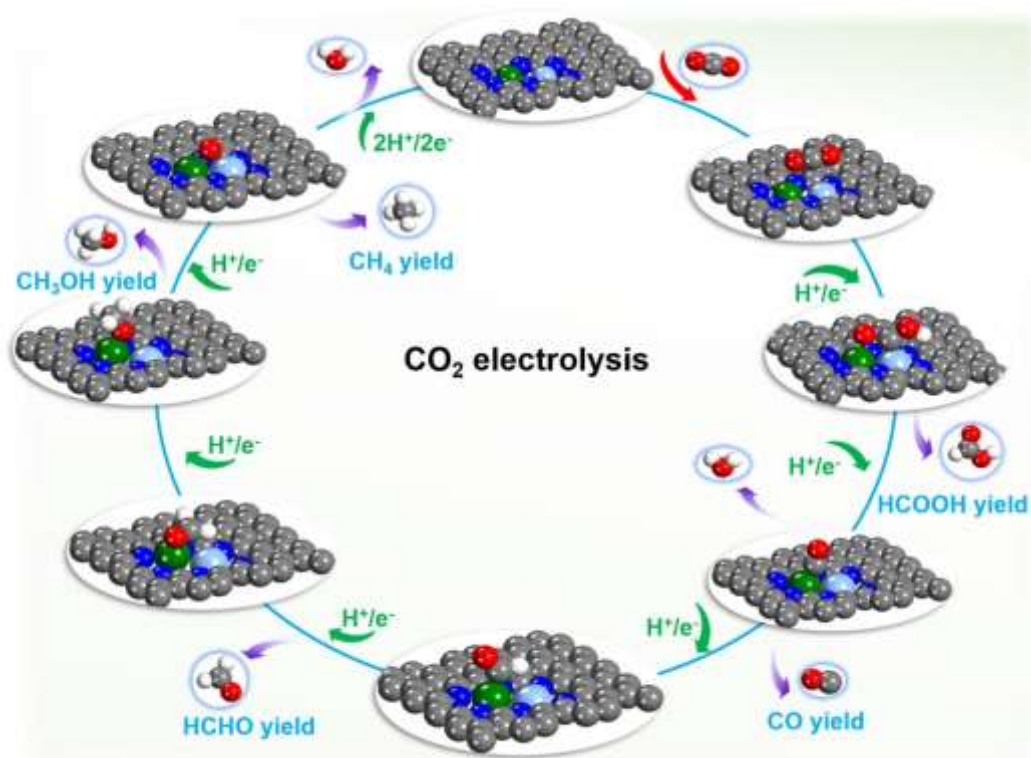
8

9   **Fig. 4.** Comprehensive reaction network for the CO_2 reduction pathway toward a variety of C1

10 products, namely, CO, HCOOH, HCHO, CH$_3$OH, and CH$_4$, on N6V4-Pd$_2$, N6V4-AgCr, N6V4-

11 AgPd, and N6V4-NiPd.

1   The overall formula for the formation of each product is provided in the supporting

2 information, i.e., Eqs. (1–15). The dual-metal active centers significantly break the

3 *CO–*CHO scaling relation; the RDS values of all the candidates are not Eq. (8) [*CO

4 $+ H^+ + e^- \rightarrow$ *CHO (*COH) $+ H_2O$], which is always the RDS for single-atom

5 catalysts.[14-15] The production of CO occurs through the path of Eq. (4) [$CO_2 \rightarrow$ *COOH

6 $\rightarrow$ CO]. The free energies of *CO_2 hydrogenation to form *COOH are increased by

7 0.78 eV (N6V4-AgPd), 0.38 eV (N6V4-AgCr), and 0.74 eV (N6V4-NiPd). This step is

8 also the RDS for producing CH_4, and the corresponding overpotential is only 0.55 V

9 for N6V4-AgCr, which is considerably lower than those of pure transition metal

10 surfaces (such as theoretical overpotential on Cu surface is 0.91 V).[57] However, the

11 desorption of CO is found to be difficult for all the candidates due to the strong

12 adsorption. In the reaction pathway of Eq. (1), i.e., [$CO_2 + 2H^+ + 2e^- \rightarrow$ HCOOH], CO_2

13 is hydrogenated by a proton–electron pair to form *COOH, and then HCOOH generated

14 via a second proton–electron pair transfers to *COOH. Only N6V4-AgPd is favorable

15 for producing HCOOH and the RDS is still the first hydrogenation of *CO_2 with a

16 change of free energy of 0.78 eV, as shown in **Fig. 5c**. The key step in the formation of

17 deep reduction products with more than $2e^-$ reduction, namely, formaldehyde (HCHO),

18 CH_3OH, and CH_4, is *CO hydrogenated to form *CHO. However, the hydrogenation

19 of *CO is not the RDS in our studied candidates due to the breaking of *CO–*CHO

20 scaling relations. For N6V4-Pd_2 and N6V4-NiPd shown in **Figs. 5b and 5d**, the

21 hydrogenation of *CO is extremely easy with decreasing free energy. For the

22 subsequent elementary reaction, i.e., Eq. (11) [*CHO $+ H^+ + e^- \rightarrow$ *OCH_2 (*CHOH)],

23 *CHO is hydrogenated to form *OCH_2 apart from *CHOH due to the relatively lower

input energy for $*OCH_2$ formation. Eq. (11) is the energy consumption step for N6V4-Pd_2, with an increase of 0.59 eV free energy, and is also the RDS in the formation of the deep reduction product, namely, CH_3OH. However, the excessive binding strength between the intermediates and N6V4-Pd_2 leading higher potentials for products desorption. $*CHO$ hydrogenation on N6V4-NiPd is likely to proceed with Eq. (9) $[*CHO + H^+ + e^- \rightarrow HCHO]$ and HCHO as a final product ($\Delta G_{max} = 0.74$ eV), as shown in **Fig. 5d**. Then, the reaction proceeds with Eq. (12) $[*OCH_2 + H^+ + e^- \rightarrow *OCH_3]$, where the C atom becomes saturated, and the C–metal bond dissociates with the O atom that was directly connected at the bridge site of the metal dimer. The next proton–electron transfer leads to the dissociation of the C–O bond and the production of CH_4. In addition, the CO_2RR pathways to CH_4 are less competitive only for N6V4-AgCr due to the energetically disfavored intermediates along the reaction path toward its formation (**Fig. 5a**). The introduction of AgCr dual-atom sites successfully reduces the change of free energy (ΔG) of $*CO$ hydrogenation without increasing the ΔG of other elementary reactions. Therefore, breaking scaling relations by designing multiple active sites might be a universal method for catalyst development.

The thermodynamic limiting potentials toward C1 products, including CO, HCOOH, HCHO, CH_3OH, and CH_4, are summarized in **Fig. 5**. The AgCr dimer exhibits extremely lower required potential toward CH_4 and HCOOH and higher potential toward other C1 productions (**Fig. 5a**). The proton–electron transfer of $*COOH$ results in lower change of free energy (ΔG) of $*CO$ hydrogenation without increasing ΔG, and the trend of HCOOH formation is upward. This finding indicates that the AgCr dimer exhibits higher efficiency and selectivity in generating CH_4. The

1   limiting potentials toward all the C1 products on the AgPd (0.78 eV) (**Fig. 5c**) and NiPd

2   (0.74 eV) (**Fig. 5d**) dimers, which both occur during the first hydrogenation (Eq. 2), are

3   relatively high. Similar limiting potentials toward different products suggesting poor

4   selectivity. Meanwhile, the Pd_2 dimer exhibits relatively better selectivity toward the

5   HCOOH product with a significantly low limiting potential (0.37 eV) (**Fig. 5b**). While

6   for deep reduction to produce CH_4, it exhibits lower efficiency and selectivity. We also

7   calculated all reaction paths for CO_2 reduction to CH_4 of single metal catalysts based

8   on the candidates of dual-metal atoms catalysts, including AgN4,
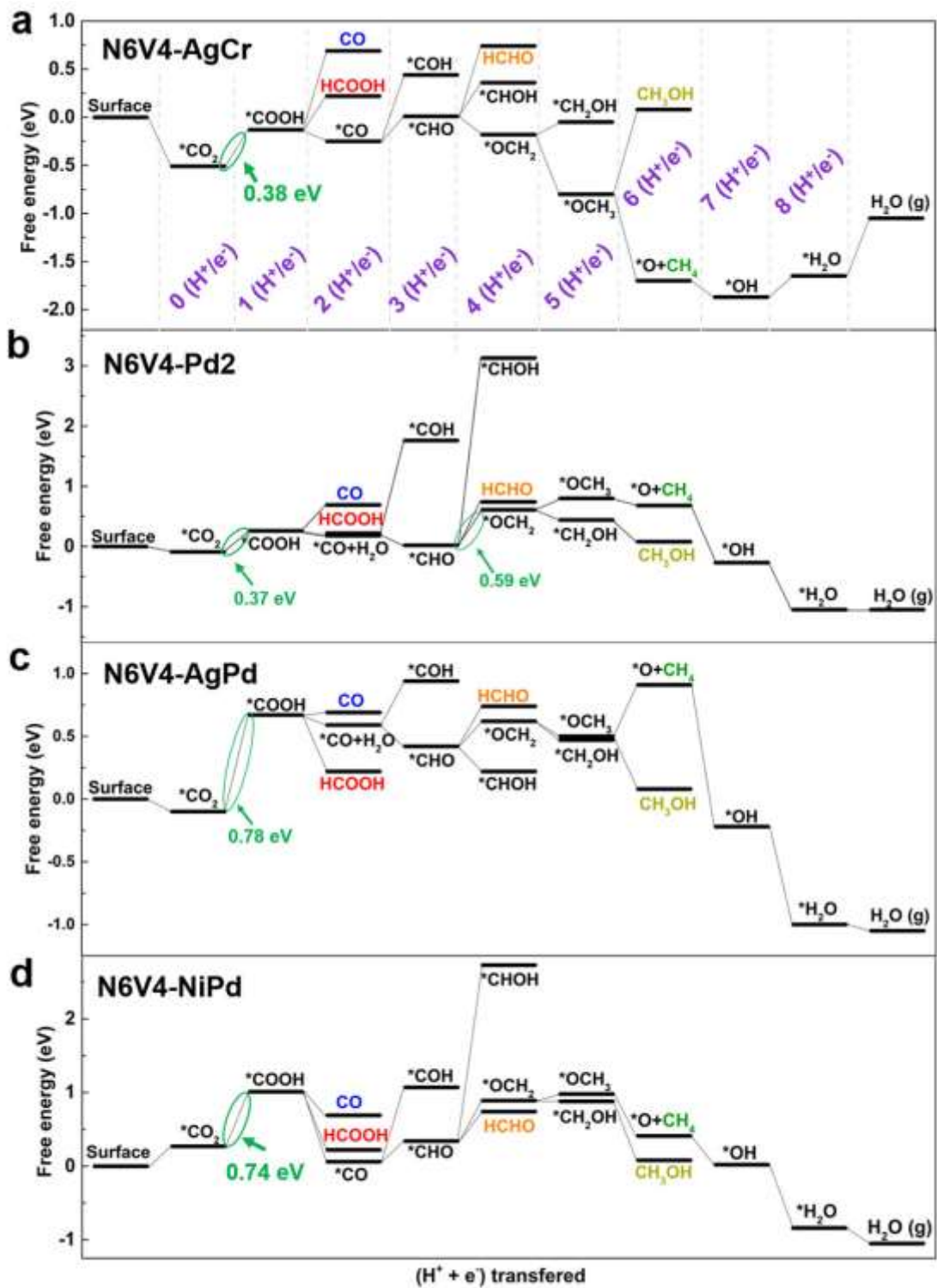
**Fig. 5.** Free energy profiles for CO_2 reduction reaction to CO, HCOOH, HCHO, CH₄, and

1   CH_3OH on (a)N6V4-AgCr, (b) N6V4-Pd2, (c) N6V4-AgPd and (d) N6V4-NiPd at zero applied

2   voltage (vs. RHE).

3   PdN4, CrN4, and NiN4. The entire reaction paths are shown in **Fig. S5**. The CO_2

4   reduction performances of single sites are not good enough compared with that of dual

5   metal sites, which show poor selectivity and high overpotentials. The limiting potentials

6   for CrN_4, NiN_4, PdN_4 and AgN_4 are -0.71, -1.50, -1.78 and -2.01 eV, respectively. These

7   results are all higher than that of our corresponding dual-metal atoms in N doped

8   graphene (-0.38 eV for AgCr, -0.59 eV for Pd2, -0.78 eV for AgPd, and -0.74 eV for

9   NiPd). It can also be seen from **Fig. S5** that the rate-determining steps all occur in the

10   first hydrogenation step of the reaction process except for CrN4. The above results

11   indicated that the activity of single sites in our manuscript is not good enough compare

12   with dual metal sites.

13   **3.4 CO_2RR versus HER**

14   An ideal catalyst for CO_2RR except high stability and activity, should also be able

15   to effectively suppress HER to achieve high FE. Therefore, the next step is to judge the

16   catalytic selectivity of the screened catalysts. In this context, we calculate the limiting

17   potential between CO_2RR and HER [$U_L(CO_2RR) - U_L(HER)$] to estimate the catalytic

18   selectivity of different catalysts. The $U_L(CO_2RR) - U_L(HER)$ versus $U_L(CO_2RR)$

19   relationship of the four promising CO_2RR catalysts is presented in **Fig. 6**. The results

20   indicate that N6V4-AgCr is located at the top right corner of **Fig. 6**, indicating its

21   superior catalytic activity and excellent CO_2RR catalytic selectivity. Compared with the

22   adsorption energy of *H on the metal site of N6V4-AgCr (−0.80 eV), CO_2 adsorption

23   (−0.91 eV) is more negative. Consequently, the adsorption of CO_2 is preferre and the

1   adsorption of H is hampered. However, N6V4-AgPd and N6V4-NiPd may not be

2   favorable in the competition with H evolution, leading to poor CO_2RR selectivity. For

3   N6V4-Pd$_2$, the adsorption energy of *H at the metal site (-1.00 eV) is more negative

4   than that of *CO_2 (-0.45 eV), also indicating poor CO_2RR selectivity.
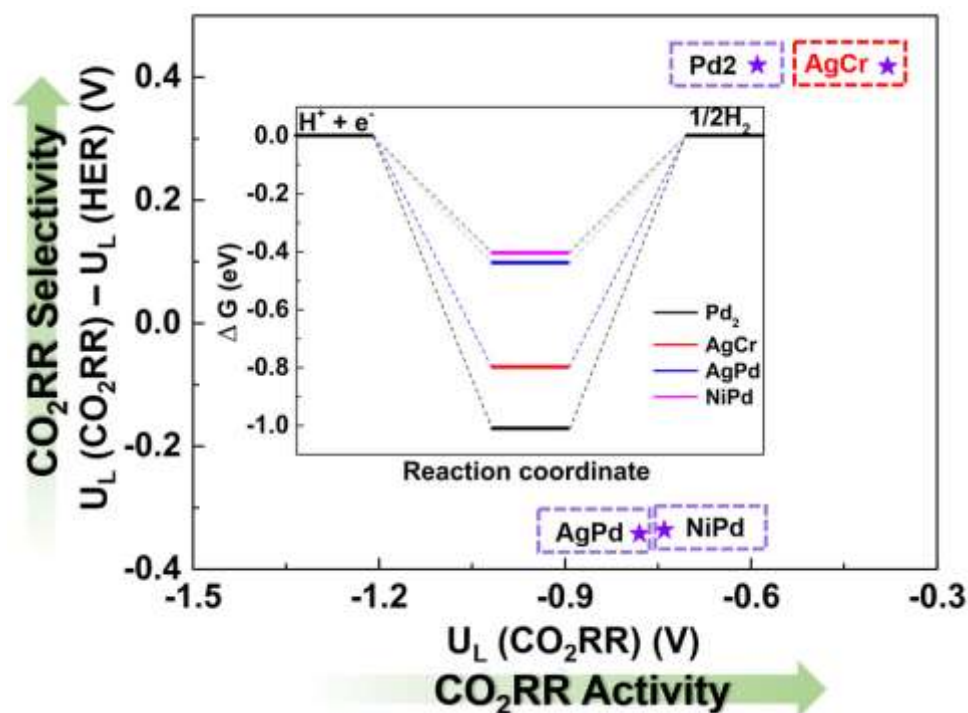
6   **Fig. 6.** Limiting potential [$U_L(CO_2RR)$] vs. $U_L(CO_2RR) - U_L(HER)$, suggesting the CO_2RR

7   activity and selectivity of the four screened catalysts. The inset figure is the free energy

8   diagrams of HER.

9   **3.5 Activity origin**

10   What factor is responsible for the difference in dual-metal-dependent CO_2RR

11   performance? To decode the underlying mechanism, electronic structures are analyzed

12   by calculating the electron localized function (ELF) and electrostatic potential (ESP) of

13   the four candidates. In **Fig. S6**, the ELF maps show that the electrons around C and N

are highly localized and delocalized regions existing around metals. Therefore, the two

metals in the middle can be inferred to be in the ionic state and a strong covalent bond

is formed between C–N and C–C. The primary interaction between metal ions and N

atoms is Coulombic attraction, which can be inferred from the lone pair between the

metal ions and the N atoms (the red regions). Furthermore, the classic Lewis acid-base

could be found at the metal ions and adjunct N, while the metals and their para-N atom

(the green arrow in Fig. 7a-d) show a distance from 4.169 to 4.556 Å. Because two

metal atoms of the dual-atomic systems are out of the substrate, the interaction between

metal and their para-N atom is regarded as deliver FLP-like activity (as shown by the

green arrow in Fig.7 a-d.). Electron transfer between CO_2 and Lewis pairs contributes

to the Lewis acid activity of Lewis pairs.[58-59] Obviously, the bond length of Ag-N and

Cr-N in N6V4-AgCr is 4.556 and 4.177 Å, respectively. Meanwhile, the bond length of

Ag-N and Pd-N in N6V4-AgPd, Ni-N and Pd-N in N6V4-NiPd, Pd1-N（Pd2-N） in

N6V4-Pd2, is 4.350, 4.437, 4.387, 4.252, and 4.169(4.303) Å, respectively. In a nutshell,

we can make a conclusion that the enhanced acidity and basicity of Lewis sites together

with the elongated distance of Lewis pairs (Ag$\cdots$N, 4.556 Å) contribute to the highest

CO_2RR activity. The associative activation of CO_2 on FLPs experiences a adsorption

and hydrogenated pathway $[(*CO_2)\delta- + (H^+)\delta+ + e^-]\rightarrow$ *COOH) with a moderate

adsorption and low activation energy of 0.38 eV on N6V4-AgCr.

Although FLPs exist in all dual-metal candidates, the activity of FLPs also varies

in different diatomic systems due to the difference in the d-orbital electronic

arrangement of various transition metals. **Fig. 7** clearly shows the ESP distribution on

different atoms. The reddish region has a lower ESP and is more susceptible to attacks

by electrophilic reagents. The blue area has a high ESP and is susceptible to

nucleophilic reagent assault. Nearly all the N atoms are red, indicating low ESP.

1 Compared with N6V4-Pd2, N6V4-AgPd, and N6V4-NiPd, the Ag atom of N6V4-AgCr

2 demonstrates a stronger charge contraction by adjacent Cr cations because the d-orbital

3 of Cr is in a semi-full state, and thus, losing electrons is easier than that in the fully

4 charged state of the d-orbital of Ag. Bader charge analysis further indicates that the Ag

5 of N6V4-AgCr is positively charged by approximately $0.59e^-$ loss and Cr shows a

6 higher positive charge (1.20 e^-) than all other metal atoms, suggesting higher capability

7 to activate CO_2 molecules.[60]
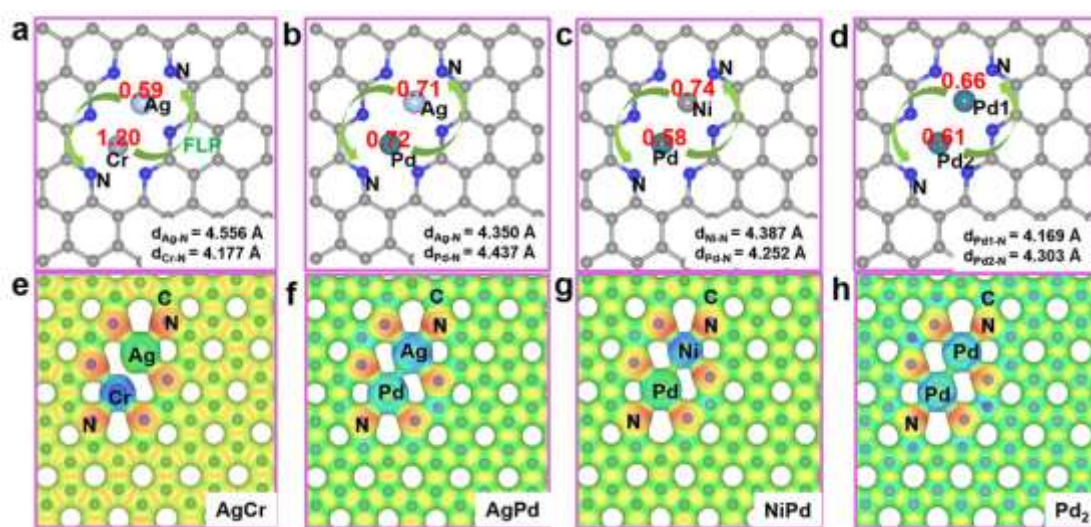
8

9 **Fig. 7.** Schematic of the design concept for FLPs in the N6V4-M1M2/M_2 crystal structure. (a–

10 d) Optimized structures of N6V4-Pd2, N6V4-AgCr, N6V4-AgPd, and N6V4-NiPd. The red

11 number indicates the lost Bader charge for each metal. (e–h) Corresponding electron density of

12 the four candidates. Electron density isosurfaces are plotted at 0.07 e bohr^{-3}. The reddish region

13 has a lower electrostatic potential and is more susceptible to attacks by electrophilic reagents.

14 The bluer the area, the higher the ESP, and the easier it will be for nucleophilic reagents to

15 attack the area.

3.6 *d*-Orbital spin-split rule

In order to reveal the internal mechanism of the above results, the projected density of states (PDOS) of above four candidates was compared (**Fig. 8**). Previous literatures have mentioned that spin polarization of transition metals will affect the adsorption of small molecules. [61-62] For example, the interaction of surface Mn atoms makes it produce strong spin polarization, which promotes the breaking of N-N triple bond and promoting subsequent reactions.[61] In addition, the spin polarization (1.38, 2.18, 1.07, 2.05, and 2.85 μB for Nb, Mo, Ta, W, and Re on g-CN, respectively) is obviously quenched after N_2 adsorption, benefitting to the activation of N_2.[62] In our case, activation of the CO_2 molecules is the first step of the CO_2RR. CO_2 consists of two σ bonds (generated from the sp hybrid orbital of the carbon atom and the p orbital of oxygen) and two delocalized π bonds (Two p-orbitals of carbon atoms which are not involved in hybridization overlap with p-orbitals of oxygen atoms side by side). Since the oxygen atom has a high electronegativity, the electron reactivity of the two pairs of highest occupied orbitals is strong, resulting in low chemical activity of the CO_2 molecule. By forming chemical bonds between CO_2 and the active sites of the catalyst, electrocatalysts stabilize CO_2 radicals or intermediates, resulting in a lower redox potential.[63] Furthermore, since CO_2 has an empty orbit with a lower energy level and a higher electron affinity, it accepts electrons easily.[64] Therefore, a catalyst with a strong ability to lose electrons will help the adsorption and activation of CO_2. The spin polarization (3.269 μB) is obviously seen only for N6V4-AgCr, benefitting to the activation of CO_2.[62] While there is no spin polarization observed on N6V4-AgPd, N6V4-NiPd and N6V4-Pd2. We further calculated the PDOS of all the stable diatomic structure combined with Ag, as shown in **Fig. S7**. It revealed that the degree of electron spin polarization gradually decreases as the atomic number increases, such as the spin

1 polarization of N6V4-AgCr is the largest (3.269 μB), while the spin polarization of

2 AgFe and AgCo are gradually decrease to 1.848 and 0.590 μB, respectively. In

3 comparison, AgNi, AgCu and AgPd show high spin symmetry.
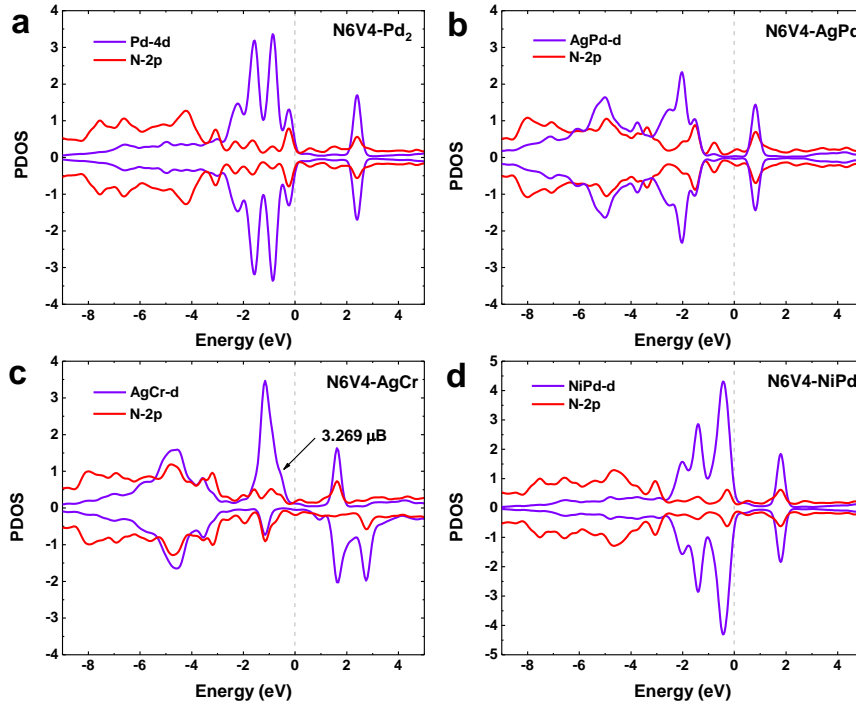

5 **Fig. 8.** Partial density of states (PDOS) of metals and N on (a) N6V4-Pd$_2$, (b) N6V4-AgPd, (c)

6 N6V4-AgCr, and (d) N6V4-NiPd before the adsorption of CO_2. Fermi level is set to be 0 eV.

7   Furthermore, the local density of states (LDOS) is adopted to disclose the effect

8 of the interaction between different metals on the spin polarization of d orbital electrons

9 compared with the bulk structure of each metal. Take N6V4-AgCr as a consideration

10 as shown in **Fig. S8**, the bulk structures of Ag and Cr metals show octahedral

11 coordination field that d_{xy}, d_{xz} and d_{yz} triple-fold degenerated into one orbital, and d_{x2-y2}

12 $_{y2}$ and d_{z2} are double-fold degenerated into another orbital alone. However, when Ag

13 and Cr form a diatomic structure and coordinate with N, the degenerated d orbitals of

14 Ag and Cr are simultaneously splitting into five sub-bands of different energy levels

1 and accompanied with the peak shift. Upon polarization as shown in **Fig. 9**, the d-orbital

2 produces five higher-energy spin-down d-orbitals and five lower-energy spin-up

3 orbitals. The electron arrangements of Cr are $d^n = 5$ with the outermost electron

4 arrangement: $3d^54s^1$. Spin-up d-orbitals are partially occupied (see **Fig. S8d** for details),

5 i. e. both the LUMO (around 1.8 eV) and HOMO (around -1.5 eV) consist of spin-up

6 d-orbitals and leave the remaining spin-down d-orbitals empty (from -3.5 ~ 1.8 eV).

7 While the outermost electron arrangement of Ag is $4d^{10}5s^1$ and only d_{xy} orbital of Ag

8 shows the spin polarization (see **Fig. S8b** for details). Both spin-up and spin-down d_{xy}-

9 orbital occupied the LUMO (around 1~3 eV) and HOMO (around -2~0.5 eV),

10 respectively. The result also coordinated with the symmetry matching rule of the

11 frontier orbitals of M-d and CO_2-σ/CO_2-π*, which further illustrates the electron

12 acceptance and donation as shown in **Fig. 9.** N6V4-AgCr has more empty d orbitals

13 and a high spin polarization to accept electrons and hence leads to the stronger CO_2

14 adsorption to initiate the reaction. While for AgPd (**Fig. S9**), NiPd (**Fig. S10**) and Pd_2

15 (**Fig. S11**) diatomic structures, they will also lead to the splitting of the d orbital, but

16 there is no spin polarization due to the higher occupations of d orbitals. Hence, CO_2

17 molecules will be favorably adsorbed onto the surface of N6V4-AgCr, and the

18 subsequent hydrogenation processes, i.e., Eqs. (1) – (13), will proceed successfully.

19 Based on above analysis, we found that the combination of different diatoms will lead

20 to differences in the arrangement of metal d orbitals, and this difference causes various

21 electron spins polarization and thus affects the selectivity and performance of catalysis.
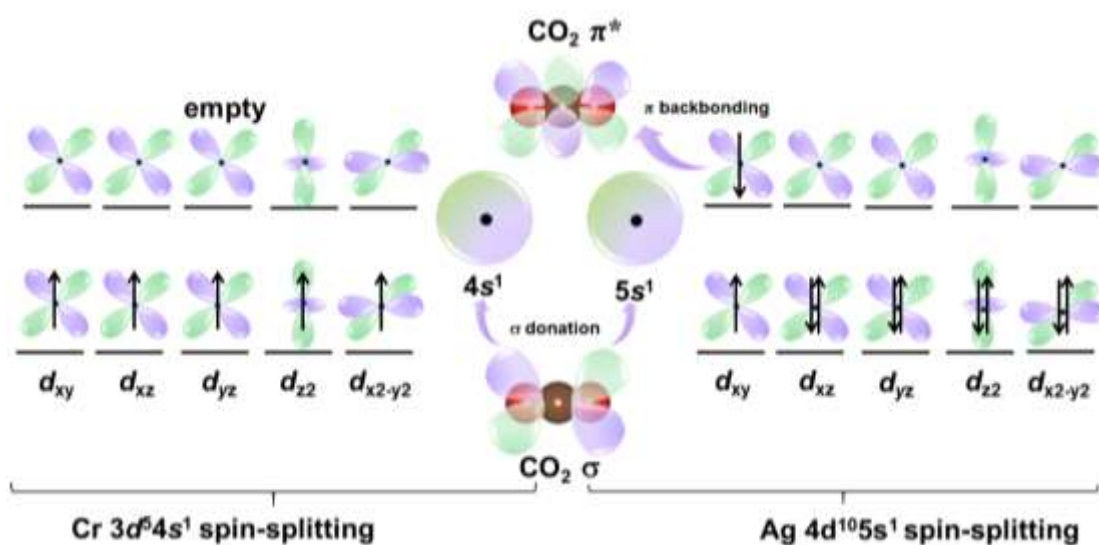
Fig. 9. Electronic configurations of spin-split d-orbitals for Cr and Ag to generate the empty spin-down higher-energy d-orbitals of Cr or the all fully spin-up and partially spin-down d-orbitals of Ag, respectively. The arrows along different directions represent electrons with opposite spins. The CO_2 in the middle shows the relationship between the bonding state and the anti-bonding state of CO_2 and the outermost electrons of the metal.

4. Conclusions

In summary, we examined the potential of dual-metal atoms embedded into N-doped graphene, named, N6V4-M$_2$ and N6V4-M1M2, as efficient CO$_2$RR electrocatalysts via high-throughput first-principles screening. We systematically studied 36 systems. Our results indicated that half systems were first excluded as qualified candidates that meet the screening criteria of thermodynamic and electrochemical stabilities. Subsequently, only four systems were selected due to the significant deviations from linear scaling relations. Lastly, N6V4-AgCr was found to exhibit superior catalytic activity and selectivity toward CH$_4$ production with an extremely low overpotential of 0.55 V. Electronic structure analysis demonstrated that

the FLPs formed between the metal and the para-N leads to a difference in the spin polarization of the systems, affecting catalytic performance. Overall, this work provides a comprehensive understanding for screening and designing novel DMACs with the stability, activity, and selectivity. We believe this research will motivate additional experimental and theoretical studies to further explore ideal catalysts for CO_2 electroreduction.

Conflicts of interest

There are no conflicts to declare.

Supporting Information

Additional computational details, representative pathways of each products, optimized structures of all systems, the value of formation energy and dissolution potential for all systems, and the density of states of four candidates

Acknowledgements

Technology Office (ICTO) at University of Macau.

References

1. Liu, M.; Pang, Y.; Zhang, B.; De Luna, P.; Voznyy, O.; Xu, J.; Zheng, X.; Dinh, C. T.; Fan, F.; Cao, C., et al., Enhanced Electrocatalytic Co2 Reduction Via Field-Induced Reagent Concentration. *Nature* **2016**, *537*, 382-386.

2. Voiry, D.; Shin, H. S.; Loh, K. P.; Chhowalla, M., Low-Dimensional Catalysts for Hydrogen Evolution and Co2 Reduction. *Nat. Rev. Chem.* **2018**, *2*.

3. Sheng, W.; Kattel, S.; Yao, S.; Yan, B.; Liang, Z.; Hawxhurst, C. J.; Wu, Q.; Chen, J. G., Electrochemical Reduction of Co2 to Synthesis Gas with Controlled Co/H-2 Ratios. *Energ. Environ. Sci.* **2017**, *10*, 1180-1185.

4. Nielsen, D. U.; Hu, X.-M.; Daasbjerg, K.; Skrydstrup, T., Chemically and Electrochemically Catalysed Conversion of Co2 to Co with Follow-up Utilization to Value-Added Chemicals. *Nat. Catal.* **2018**, *1*, 244-254.

5. Zheng, X.; Ji, Y.; Tang, J.; Wang, J.; Liu, B.; Steinruck, H.-G.; Lim, K.; Li, Y.; Toney, M. F.; Chan, K., et al., Theory-Guided Sn/Cu Alloying for Efficient Co2 Electroreduction at Low Overpotentials. *Nat. Catal.* **2019**, *2*, 55-61.

6. Jiao, J. Q.; Lin, R.; Liu, S. J.; Cheong, W. C.; Zhang, C.; Chen, Z.; Pan, Y.; Tang, J. G.; Wu, K. L.; Hung, S. F., et al., Copper Atom-Pair Catalyst Anchored on Alloy Nanowires for Selective and Efficient Electrochemical Reduction of Co2. *Nature Chemistry* **2019**, *11*, 222-228.

7. Kuang, M.; Wang, Q. H.; Han, P.; Zheng, G. F., Cu, Co-Embedded N-Enriched Mesoporous Carbon for Efficient Oxygen Reduction and Hydrogen Evolution Reactions. *Advanced Energy Materials* **2017**, *7*.

8. Wang, L. M.; Chen, W. L.; Zhang, D. D.; Du, Y. P.; Amal, R.; Qiao, S. Z.; Bf, J. W.; Yin, Z. Y., Surface Strategies for Catalytic Co2 Reduction: From Two-Dimensional Materials to Nanoclusters to Single Atoms. *Chemical Society Reviews* **2019**, *48*, 5310-5349.

9. Fan, K.; Jia, Y. F.; Ji, Y. F.; Kuang, P. Y.; Zhu, B. C.; Liu, X. Y.; Yu, J. G., Curved Surface Boosts Electrochemical Co2 Reduction to Formate Via Bismuth Nanotubes in a Wide Potential Window. *Acs Catalysis* **2020**, *10*, 358-364.

10. Nitopi, S.; Bertheussen, E.; Scott, S. B.; Liu, X.; Engstfeld, A. K.; Horch, S.; Seger, B.; Stephens, I. E. L.; Chan, K.; Hahn, C., et al., Progress and Perspectives of Electrochemical Co2 Reduction on Copper in Aqueous Electrolyte. *Chem. Rev.* **2019**, *119*, 7610-7672.

11. Xu, S.; Carter, E. A., Theoretical Insights into Heterogeneous (Photo)Electrochemical Co2 Reduction. *Chem. Rev.* **2019**, *119*, 6631-6669.

12. Li, F.; Li, Y. C.; Wang, Z.; Li, J.; Nam, D.-H.; Lum, Y.; Luo, M.; Wang, X.; Ozden, A.; Hung, S.-F., et al., Cooperative Co2-to-Ethanol Conversion Via Enriched Intermediates at Molecule–Metal Catalyst Interfaces. *Nat. Catal.* **2019**, *3*, 75-82.

13. Wang, W.; Qu, Z.; Song, L.; Fu, Q., Co2 Hydrogenation to Methanol over Cu/Ceo2 and Cu/Zro2 Catalysts: Tuning Methanol Selectivity Via Metal-Support Interaction. *J. Energy Chem.* **2020**, *40*, 22-30.

14. Abild-Pedersen, F.; Greeley, J.; Studt, F.; Rossmeisl, J.; Munter, T. R.; Moses, P. G.; Skulason, E.; Bligaard, T.; Norskov, J. K., Scaling Properties of Adsorption Energies for Hydrogen-Containing Molecules on Transition-Metal Surfaces. *Phys. Rev. Lett.* **2007**, *99*, 016105.

15. Calle-Vallejo, F.; Loffreda, D.; Koper, M. T. M.; Sautet, P., Introducing Structural Sensitivity into Adsorption-Energy Scaling Relations by Means of Coordination Numbers. *Nat. Chem.* **2015**, *7*, 403-410.

16. Kuhl, K. P.; Cave, E. R.; Abram, D. N.; Jaramillo, T. F., New Insights into the Electrochemical Reduction of Carbon Dioxide on Metallic Copper Surfaces. *Energ. Environ.Sci.* **2012**, *5*, 7050-7059.

17. Whipple, D. T.; Kenis, P. J. A., Prospects of Co2 Utilization Via Direct Heterogeneous Electrochemical Reduction. *J. Phys. Chem. Lett.* **2010**, *1*, 3451-3458.

18. Ooka, H.; Figueiredo, M. C.; Koper, M. T. M., Competition between Hydrogen Evolution and Carbon Dioxide Reduction on Copper Electrodes in Mildly Acidic Media. *Langmuir* **2017**, *33*, 9307-9313.

19. Li, L.; Li, B.; Guo, H.; Li, Y.; Sun, C.; Tian, Z.; Chen, L., Synergistic Effects of Heteroatom-Decorated Mxene Catalysts for Co Reduction Reactions. *Nanoscale* **2020**, *12*, 15880-15887.

20. Li, L.; Wang, X.; Guo, H.; Yao, G.; Yu, H.; Tian, Z.; Li, B.; Chen, L.,

Theoretical Screening of Single Transition Metal Atoms Embedded in Mxene Defects as Superior Electrocatalyst of Nitrogen Reduction Reaction. *Small Methods* **2019**, *1900337*, 1-7.

21. Liu, L.; Corma, A., Metal Catalysts for Heterogeneous Catalysis: From Single Atoms to Nanoclusters and Nanoparticles. *Chem. Rev.* **2018**, *118*, 4981-5079.

22. Liu, J.-C.; Xiao, H.; Li, J., Constructing High-Loading Single-Atom/Cluster Catalysts Via an Electrochemical Potential Window Strategy. *J. Amer. Chem. Soc.* **2020**, *142*, 3375-3383.

23. Yang, X.-F.; Wang, A.; Qiao, B.; Li, J.; Liu, J.; Zhang, T., Single-Atom Catalysts: A New Frontier in Heterogeneous Catalysis. *Acc. Chem. Res.* **2013**, *46*, 1740-1748.

24. Zhong, M.; Tran, K.; Min, Y.; Wang, C.; Wang, Z.; Dinh, C. T.; De Luna, P.; Yu, Z.; Rasouli, A. S.; Brodersen, P., et al., Accelerated Discovery of Co2 Electrocatalysts Using Active Machine Learning. *Nature* **2020**, *581*, 178-183.

25. Huang, Q.; Liu, H.; An, W.; Wang, Y.; Feng, Y.; Men, Y., Synergy of a Metallic Nico Dimer Anchored on a C2n–Graphene Matrix Promotes the Electrochemical Co2 Reduction Reaction. *ACS Sustain. Chem. Eng.* **2019**, *7*, 19113-19121.

26. Ouyang, Y.; Shi, L.; Bai, X.; Li, Q.; Wang, J., Breaking Scaling Relations for Efficient Co2 Electrochemical Reduction through Dual-Atom Catalysts. *Chem. Sci.* **2020**, *11*, 1807-1813.

27. Li, R.; Wei, Z.; Gou, X., Nitrogen and Phosphorus Dual-Doped Graphene/Carbon Nanosheets as Bifunctional Electrocatalysts for Oxygen Reduction and Evolution. *Acs Catalysis* **2015**, *5*, 4133-4142.

28. Li, Z.; He, H.; Cao, H.; Sun, S.; Diao, W.; Gao, D.; Lu, P.; Zhang, S.; Guo, Z.; Li, M., et al., Atomic Co/Ni Dual Sites and Co/Ni Alloy Nanoparticles in N-Doped Porous Janus-Like Carbon Frameworks for Bifunctional Oxygen Electrocatalysis. *Appl. Catal. B-Environ.* **2019**, *240*, 112-121.

29. Zheng, Y.; Jiao, Y.; Zhu, Y.; Cai, Q.; Vasileff, A.; Li, L. H.; Han, Y.; Chen, Y.; Qiao, S. Z., Molecule-Level G-C3n4 Coordinated Transition Metals as a New Class of Electrocatalysts for Oxygen Electrode Reactions. *J. Amer. Chem. Soc.* **2017**, *139*, 3336-3339.

30. Wang, J.; Gan, L.; Zhang, W.; Peng, Y.; Yu, H.; Yan, Q.; Xia, X.; Wang, X., In Situ Formation of Molecular Ni-Fe Active Sites on Heteroatom-Doped Graphene as a Heterogeneous Electrocatalyst toward Oxygen Evolution. *Sci. Adv.* **2018**, *4*, 1-8.

31. Jia, C.; Ren, W.; Chen, X.; Yang, W.; Zhao, C., (N, B) Dual Heteroatom-Doped Hierarchical Porous Carbon Framework for Efficient Electroreduction of Carbon Dioxide. *ACS Sustain. Chem. Eng.* **2020**, *8*, 6003-6010.

32. Li, Y.; Chen, C.; Cao, R.; Pan, Z.; He, H.; Zhou, K., Dual-Atom Ag-2/Graphene Catalyst for Efficient Electroreduction of Co2 to Co. *Appl. Catal. B-Environ.* **2020**, *268*, 1-10.

33. Zhao, J.; Zhao, J.; Li, F.; Chen, Z., Copper Dimer Supported on a C2n Layer as an Efficient Electrocatalyst for Co2 Reduction Reaction: A Computational Study. *J. Phys. Chem. C* **2018**, *122*, 19712-19721.

34. Luo, G.; Jing, Y.; Li, Y., Rational Design of Dual-Metal-Site Catalysts for Electroreduction of Carbon Dioxide. *J. Mater. Chem. A* **2020**.

35. Li, H.; Zhao, Z.; Cai, Q.; Yin, L.; Zhao, J., Nitrogen Electroreduction Performance of Transition Metal Dimers Embedded into N-Doped Graphene: A Theoretical Prediction. *J. Mater. Chem. A* **2020**, *8*, 4533-4543.

36. Guo, X.; Gu, J.; Lin, S.; Zhang, S.; Chen, Z.; Huang, S., Tackling the Activity and Selectivity Challenges of Electrocatalysts toward the Nitrogen Reduction Reaction Via Atomically Dispersed Biatom Catalysts. *J. Amer. Chem. Soc.* **2020**, *142*, 5709-5721.

37. Zhang, X.; Chen, A.; Zhang, Z.; Zhou, Z., Double-Atom Catalysts: Transition Metal Dimer-Anchored C2n Monolayers as N2 Fixation Electrocatalysts. *J. Mater. Chem. A* **2018**, *6*, 18599-18604.

38. He, Z.; He, K.; Robertson, A. W.; Kirkland, A. I.; Kim, D.; Ihm, J.; Yoon, E.; Lee, G.-D.; Warner, J. H., Atomic Structure and Dynamics of Metal Dopant Pairs in Graphene. *Nano Lett.* **2014**, *14*, 3766-3772.

39. Wang, J.; Huang, Z.; Liu, W.; Chang, C.; Tang, H.; Li, Z.; Chen, W.; Jia, C.; Yao, T.; Wei, S., et al., Design of N-Coordinated Dual-Metal Sites: A Stable and Active Pt-Free Catalyst for Acidic Oxygen Reduction Reaction. *J. Amer. Chem. Soc.* **2017**, *139*, 17281-17284.

40. Wang, Q.; Ji, Y.; Lei, Y.; Wang, Y.; Wang, Y.; Li, Y.; Wang, S., Pyridinic-N-

Dominated Doped Defective Graphene as a Superior Oxygen Electrocatalyst for Ultrahigh-Energy-Density Zn-Air Batteries. *ACS Energy Lett.* **2018**, *3*, 1183-1191.

41. Wang, Y.; Han, P.; Lv, X.; Zhang, L.; Zheng, G., Defect and Interface Engineering for Aqueous Electrocatalytic Co2 Reduction. *Joule* **2018**, *2*, 2551-2582.

42. Ye, W.; Chen, S.; Lin, Y.; Yang, L.; Chen, S.; Zheng, X.; Qi, Z.; Wang, C.; Long, R.; Chen, M., et al., Precisely Tuning the Number of Fe Atoms in Clusters on N-Doped Carbon toward Acidic Oxygen Reduction Reaction. *Chem* **2019**, *5*, 2865-2878.

43. Zhou, P.; Hou, X.; Chao, Y.; Yang, W.; Zhang, W.; Mu, Z.; Lai, J.; Lv, F.; Yang, K.; Liu, Y., et al., Synergetic Interaction between Neighboring Platinum and Ruthenium Monomers Boosts Co Oxidation. *Chem. Sci.* **2019**, *10*, 5898-5905.

44. Ren, W.; Tan, X.; Yang, W.; Jia, C.; Xu, S.; Wang, K.; Smith, S. C.; Zhao, C., Isolated Diatomic Ni-Fe Metal-Nitrogen Sites for Synergistic Electroreduction of Co2. *Angew Chem. Int. Ed. Engl.* **2019**, *58*, 6972-6976.

45. Grimme, S., Semiempirical Gga-Type Density Functional Constructed with a Long-Range Dispersion Correction. *J. Comput. Chem. Mater.* **2006**, *27*, 1787-1799.

46. Kresse, G.; Furthmuller, J., Efficient Iterative Schemes for Ab Initio Total-Energy Calculations Using a Plane-Wave Basis Set. *Phys. Rev. B* **1996**, *54*, 11169-11186.

47. Perdew, J. P.; Burke, K.; Ernzerhof, M., Generalized Gradient Approximation Made Simple. *Phys. Rev. Lett.* **1996**, *77*, 3865-3868.

48. Perdew, J. P.; Wang, Y., Pair-Distribution Function and Its Coupling-Constant Average for the Spin-Polarized Electron Gas. *Phys. Rev. B: Condens. Matter.* **1992**, *46*, 12947-12954.

49. Blochl, P. E., Projector Augmented-Ware Method. *Phys. Rev. B* **1994**, *50*, 27-30.

50. J, H.; Monkhorst; D.Pack, J., Special Points for Brillouin-Zone Integratiionns. *Phys. Rev. B* **1976**, *13*, 5188-5192.

51. Grimme, S.; Antony, J.; Ehrlich, S.; Krieg, H., A Consistent and Accurate Ab Initio Parametrization of Density Functional Dispersion Correction (Dft-D) for the 94 Elements H-Pu. *J. Chem. Phys.* **2010**, *132*, 1-19.

52. Grimme, S.; Ehrlich, S.; Goerigk, L., Effect of the Damping Function in Dispersion Corrected Density Functional Theory. *J. Comput. Chem.* **2011**, *32*, 1456-1465.

53. Li, Q.-K.; Li, X.-F.; Zhang, G.; Jiang, J., Cooperative Spin Transition of Monodispersed Fen3 Sites within Graphene Induced by Co Adsorption. *J. Amer. Chem. Soc.* **2018**, *140*, 15149-15152.

54. Greeley, J.; Norskov, J. K., Electrochemical Dissolution of Surface Alloys in Acids: Thermodynamic Trends from First-Principles Calculations. *Electrochimica Acta* **2007**, *52*, 5829-5836.

55. Shi, C.; Hansen, H. A.; Lausche, A. C.; Norskov, J. K., Trends in Electrochemical Co2 Reduction Activity for Open and Close-Packed Metal Surfaces. *Physical Chemistry Chemical Physics* **2014**, *16*, 4720-4727.

56. Hansen, H. A.; Varley, J. B.; Peterson, A. A.; Norskov, J. K., Understanding Trends in the Electrocatalytic Activity of Metals and Enzymes for Co2 Reduction to Co. *J. Phys. Chem. Lett.* **2013**, *4*, 388-392.

57. Li, Y.; Sun, Q., Recent Advances in Breaking Scaling Relations for Effective Electrochemical Conversion of Co2. *Advanced Energy Materials* **2016**, *6*.

58. Liu, L.; Lukose, B.; Ensing, B., A Free Energy Landscape of Co2 Capture by Frustrated Lewis Pairs. *ACS Catalysis* **2018**, *8*, 3376-3381.

59. Zhang, S.; Huang, Z. Q.; Ma, Y.; Gao, W.; Li, J.; Cao, F.; Li, L.; Chang, C. R.; Qu, Y., Solid Frustrated-Lewis-Pair Catalysts Constructed by Regulations on Surface Defects of Porous Nanorods of Ceo2. *Nat Commun* **2017**, *8*, 15266.

60. Chen, S.; Yuan, H.; Morozov, S. I.; Ge, L.; Li, L.; Xu, L.; Goddard, W. A., Design of a Graphene Nitrene Two-Dimensional Catalyst Heterostructure Providing a Well-Defined Site Accommodating One to Three Metals, with Application to Co2 Reduction Electrocatalysis for the Two-Metal Case. *J. Phys. Chem. Lett.* **2020**, *11*, 2541-2549.

61. Wang, S.; Li, B.; Li, L.; Tian, Z.; Zhang, Q.; Chen, L.; Zeng, X. C., Highly Efficient N-2 Fixation Catalysts: Transition-Metal Carbides M2c (Mxenes). *Nanoscale* **2020**, *12*, 538-547.

62. Niu, H.; Wang, X.; Shao, C.; Zhang, Z.; Guo, Y., Computational Screening

Single-Atom Catalysts Supported on G-Cn for N2 Reduction: High Activity and Selectivity. *ACS Sustain.Chem. Engin.* **2020**, *8*, 13749-13758.
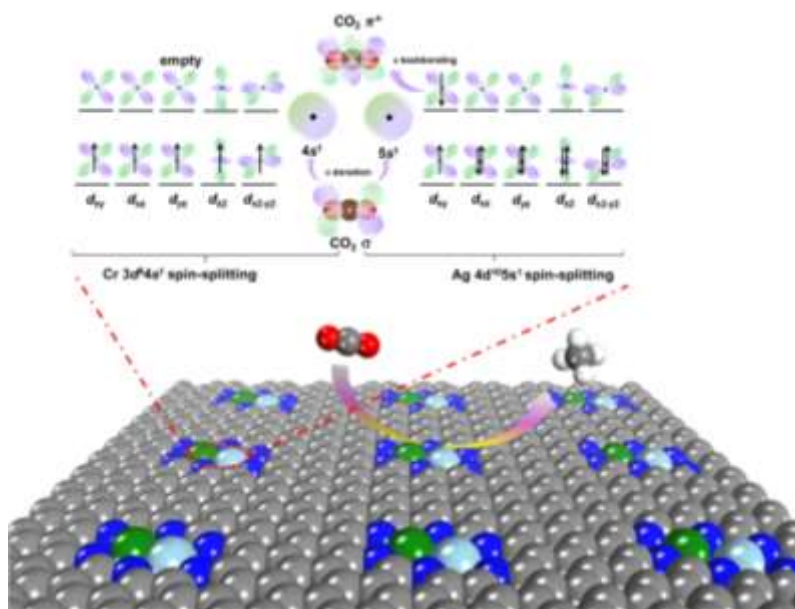
63. Chen, S.; Wang, H.; Kang, Z.; Jin, S.; Zhang, X.; Zheng, X.; Qi, Z.; Zhu, J.; Pan, B.; Xie, Y., Oxygen Vacancy Associated Single-Electron Transfer for Photofixation of Co2 to Long-Chain Chemicals. *Nat Commun* **2019**, *10*, 788.

64. Kong, Y.; Liu, D.; Ai, H.; Lo, K. H.; Wang, S.; Pan, H., Theoretical Screening of Single Atoms Supported on Two-Dimensional Nb2cn2 for Nitrogen Fixation. *ACS Applied Nano Materials* **2020**, *3*, 11274-11281.

1   TOC Graphic

2

3